A semi-analytical model for low-density impact-based surface treatments: Application to the abrasive waterjet texturing of thermoplastic polymers

Pierre Fréquelin, Redouane Zitoune, J Jumel, Sabine Le Roux, Agathe Jaillon, François Cénac

Tribology International 201 (2025) 110256

Contents lists available at ScienceDirect

Tribology International

journal homepage: www.elsevier.com/locate/triboint

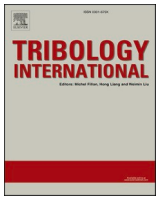

A semi-analytical model for low-density impact-based surface treatments: Application to the abrasive waterjet texturing of thermoplastic polymers

Pierre Fréquelin [a,b,c,*], Rédouane Zitoune [a,d,**], Julien Jumel [b], Sabine Le Roux [e], Agathe Jaillon [c], François Cénac [c]

[a] Institut Clément Ader (ICA), Université de Toulouse, CNRS UMR 5312, 3 Rue Caroline Aigle, 31400 Toulouse, France
[b] ENSTA Bretagne, Institut de Recherche Dupuy de Lôme, CNRS UMR 6027, 2 Rue François Verny, 29806 Brest, France
[c] BAYAB Industries, 10 Allée de Longueterre, 31850 Montrabé, France
[d] CNRS-International-NTU-THALES-Research-Alliance (CINTRA, UMI 3288), Nanyang Technological University, Singapore
[e] Institut Clément Ader (ICA), Université de Toulouse, CNRS UMR 5312, Campus Jarlard, 81013 Albi, France

ARTICLE INFO

Keywords:
Particle impact
Polymers
Roughness
Surface topography

ABSTRACT

Surface roughness is critical for bonding applications, as it directly influences the mechanisms occurring at the adhesive interface. Abrasive Waterjet texturing has emerged as a promising technique for functionalizing surfaces, but predicting the surface characteristics from stochastic impact-based processes remains a challenge. This study aimed to develop a numerical model capable of forecasting key morphological parameters for AWJ-textured surfaces with pilotable treatment coverage. The proposed model was optimized through theoretical analysis and confronted to topographical data from polymer samples treated with low-density AWJ using standard parameters. Profilometry measurements were supported by a custom post-treatment algorithm to remove artefacts and assess the characteristics of individual particle impacts (number, repartition, dimensions). The predicted roughness showed a 94 % concordance to the measured values.

1. Introduction

Many properties of a material depend on surface morphology. For instance, several researchers have shown that smoother surfaces improve the tensile strength, fatigue strength, and fatigue life of metals [1–5]. Low surface roughness has also been reported to reduce the corrosion rate of pure copper and to slow down the friction wear of chromium-based coatings [6,7]. On the other hand, surface morphology can play an important role in substrate adherence to coatings and adhesives. In fact, it has been mentioned that rough surfaces benefit from larger contact areas with the adhesive, which increases the number of physicochemical interactions available between the two phases [8]. To a lesser extent, adherence is also improved by the mechanical anchoring of the adhesive against the walls of peaks and crevices present on rough surfaces [9]. However, some optimal surface morphology should be identified for a given viscosity of the adhesive, as overpronounced asperities will not allow for a good penetration of the adhesive and lead to voids as well as stress concentration points [10–13]. Considering the adherence of thermoplastic polymers whose physicochemical affinity with adhesives is generally limited (e.g., PA, PEEK, PEKK, PTFE), it is of interest to try and optimize surface morphology so that it takes up the maximum amount of mechanical stress possible for a given adhesive.

It is important to mention that current texturing processes exhibit clear industrial limitations. For instance, sanding favours the generation of anisotropic textures and has limited precision on curved surfaces due to the heterogeneity of the applied load, while sandblasting requires complex infrastructure in order to confine the extensive amount of hazardous powder released. In addition, sandblasting often leads to the contamination of the substrate through particle embedment. Consequently, the benefits of texturing to functionalize polymer surfaces are progressively being outperformed by physical treatments (i.e., laser, plasma, and corona) and research on morphology-based adherence is losing momentum. Texturing with the Abrasive Waterjet (AWJ) process is an unexplored alternative which may be able to compete with physical processes to enhance the adherence of thermoplastic polymers. In fact, it has been shown that surface preparation with AWJ on a 3D-woven carbon-thermoset composite significantly increases the critical energy release rate (G_{Ic}) of CFRP/CFRP bonded assemblies, as compared to sanding [14]. The volume of craters below the mean plane has notably

* Corresponding author at: Institut Clément Ader (ICA), Université de Toulouse, CNRS UMR 5312, 3 Rue Caroline Aigle, 31400 Toulouse, France.
** Corresponding author at: Institut Clément Ader (ICA), Université de Toulouse, CNRS UMR 5312, 3 Rue Caroline Aigle, 31400 Toulouse, France.
E-mail addresses: p.frequelin@bayab.fr (P. Fréquelin), redouane.zitoune@iut-tlse3.fr (R. Zitoune).

https://doi.org/10.1016/j.triboint.2024.110256
Received 2 August 2024; Received in revised form 5 September 2024; Accepted 15 September 2024
Available online 16 September 2024

Nomenclature

a	projected area of indent (μm^2).
A	volume-derived projected area of indent (μm^2).
c_i	surface coverage of indents (%).
E	Young's modulus (MPa).
h	depth of indent (μm).
H	volume-derived depth of indent (μm).
n_i	number density of indents (/mm^2).
V	volume of indent (μm^3).
w_i	volume coverage of indents (μm^3/μm^2).
S_a	Arithmetical mean height (μm).
S_{sk}	Skewness of height distribution (-).
S_{ku}	Kurtosis of height distribution (-).
V_{vv}	Dale void volume (μm^3/μm^2).
S_{dr}	Developed interfacial area ratio (%).
λ	projected area of pileup (μm^2).
Λ	volume-derived projected area of pileup (μm^2).
κ_i	surface coverage of pileups (%).
ν	Poisson's ratio (-).
ζ	height of pileup (μm).
Z	volume-derived height of pileup (μm).
η	number of pileups per indent (/mm^2).
Υ	volume of pileup (μm^3).
ω_i	volume coverage of pileups (μm^3/μm^2).
ρ	absolute mass density (g/cm^3).
ρ_c	Concordance correlation coefficient (-).
Γ_i	texture parametrization set *i*.
χ_q	ratio of extrema for quantity *q*.
σ_d	standard deviation of distribution.

been identified as a possible broad predictor of interfacial adherence for AWJ treatments, with a reported change in the crack propagation behaviour as this parameter is increased. The ability of impact-based treatments to produce higher crater volumes than abrasion by sandpaper could perhaps explain the higher static joint strength that has been shown for both carbon/epoxy (thermoset) and carbon/PEEK (thermoplastic) single lap assemblies with RT-cure paste epoxy adhesives [9]. However, it is important to recall that the morphology required for optimal interfacial adherence is indissociable from the rheological properties of the adhesive. Besides, the same texturing process applied to either a thermoset or a thermoplastic substrate would likely result in dissimilar morphologies.

Most thermoplastic polymers exhibit high ductility and are therefore expected to be indented by hard particles under loading. At high strain-rates, pileups or lips are often observed above the initial surface and around the indenter. These are partly attributed to the strain-softening behaviour of the impacted material, which is thus displaced towards regions of lower mechanical resistance via the formation of shear bands [15]. When such crater geometries overlap, complex topographical structures with no apparent patterns tend to emerge. Thus, to characterize the morphological properties of such textures, it is common to refer to standardized indicators, which generally consist of statistical reductions. In most cases, profile parameters (R_a, R_q, etc.) are calculated on a selected 2D cross-section of the surface, using a contact profilometer. However, areal field parameters (S_a, S_q, etc.), which account for all the elevation points on the 3D surface, are better suited to describe random impact-based texturing, where no preferred direction is produced as on conventionally machined surfaces (turning, milling). The ISO 25178 standard defines 26 parameters to quantify the height topography and defects distribution of a surface [16]. Yet, it has been shown that many of these quantities are mostly redundant for broad-spectrum surface evaluation and that only 13 core morphological functions could be sufficient [17]. Also, different parameters may be relevant depending on the application. For instance, bearing area (S_k, S_{pk}, S_{vk}) and void volume (V_{vc}, V_{vv}) parameters can provide valuable information about the load-bearing capacity and lubricant retention properties of tribological surfaces [18]. However, identifying the appropriate topographic parameters for surface adhesion can be complex, as morphology is just one of many influencing factors. Arithmetical mean height (S_a) is by far the most common areal roughness criterion used for surface characterization for adhesive bonding applications [14]. In fact, assessing the S_a of a substrate prior to bonding is necessary to rigorously compare different texturing processes. Indeed, major performance differences between surface preparations often involve divergences in S_a [8]. However, arithmetical mean height on its own is not enough to functionally describe a surface, for the averaging operation essentially blurs important morphological features. This is especially true for tribological applications in which an extensive set of roughness parameters is generally required for reliable surface description [19]. Yet, measuring areal roughness criteria can be costly, both in time and equipment, especially with semi-transparent materials such as amorphous or semi-crystalline polymers. Therefore, means to predict S_a for a given process are almost always worth investigating, either through analytical or numerical modelling.

Numerical modelling is often a useful tool to increase the general understanding of highly coupled processes such as AWJ. For example, Anwar *et al.* [20] proposed a finite elements model that could predict the machining depth resulting from the consecutive impacts of particles in a high-density AWJ with an acceptable precision, although surface roughness was not measured nor calculated. Schwartzentruber *et al.* [21] proposed a numerical model that was able to accurately predict the arithmetic mean roughness R_a of the trims resulting from AWJ cutting of a carbon fibre reinforced epoxy resin. Their strategy consisted of saturating the surface with craters resulting from a distribution of impacts with characteristic dynamic properties. Therefore, it was designed to exclusively model machined surfaces resulting from high density treatments. Also, the accuracy of the modelled roughness was reported to significantly decrease for more ductile, thermoplastic substrates. Hence, extending the range of applications for AWJ to include surface functionalization requires to switch to an approach where the number density of craters can be piloted. There have been several successful attempts to design predictive models of roughness parameters for impact-based processes with controlled density, using either semi-analytical or finite elements methods to model the interactions between different topographical entities. Most of these originate from the shot-peening community which has laid the foundations of how impact-based textures should be conceptually approached, using the notion of surface coverage of the applied treatment, as formalized by Kirk and Abyaneh [22]. Coverage is currently accepted as the most important quantifiable variable for shot-peening treatments, first-order driving both the residual surface morphology and mechanical properties of the target [23–25]. Taro *et al.* [26] notably developed a semi-analytical model to predict 2D profile parameters resulting from a homogenous repartition of identical spherical indents for a large range of coverage values. Heydari *et al.* [27] and Senge *et al.* [28] achieved analogous results using finite elements modelling and calculated several areal field parameters with relative precision. Methods that control for surface coverage have also been applied to high-frequency hammering and laser texturing, but not grit-blasting nor AWJ for which the characterization of textures is still very much process-oriented (abrasive grade, particle energy, tool traverse velocity, etc.) [29–31]. To the best knowledge of the authors, no attempt to design a modelling procedure

applicable to any texturing process and target material, which could for example help predict the surface roughness of thermoplastic polymers textured with low-density AWJ, has yet been reported in the literature. Like most other impact-based processes and unlike laser texturing, AWJ is a stochastic process, which means that it is incapable of producing regular morphological patterns.

The present study aims to propose a simple method to accurately model an AWJ-textured surface with the lowest possible number of entry parameters. For this purpose, the surface topography resulting from low-density AWJ treatment applied on PMMA and PEKK was measured. A series of geometric and numerary parameters, relevant to describe the distribution of topographic features, was extracted using a custom post-treatment algorithm, and then injected in an original numerical model to generate simple equivalent surfaces. Finally, several key indicators of surface topology were computed and compared with experimental measurements to assess the accuracy and performance of the proposed model. The proposed model could be used to guide the selection of process parameters for texturing operations, so as to target specific roughness parameters in accordance with industrial needs. Indeed, it is common to receive orders for textured parts that should conform to a certain range of S_a (e.g., aircraft parts to be painted, for both aesthetic and aerodynamic reasons). Eventually, the model could be made available to any impact-based texturing process (AWJ, sandblasting, shot-peening, etc.), which would require a one-time identification of the relevant geometric parameters associated with a range of upstream process parameters (pressure of the carrying fluid, particle size and flowrate, etc.) and target-materials of interest. Then, the desired surface roughness could be achieved simply by varying the impact coverage via the tool's traverse velocity and/or step-over distance.

2. Experimental procedure

2.1. Materials

Two semi-crystalline thermoplastic polymers were chosen as substrates: Kepstan 7002 Poly-Ether-Ketone-Ketone (PEKK) and Altuglas Poly-Methyl-Meth-Acrylate (PMMA). However, it is important to mention that there was a significant difference in the process quality of the selected materials. The PMMA samples were moulded, commercial-grade with film protection, and appeared pristine under visual examination, whereas the PEKK samples were end-of-series extruded plates with several visible defects. This is why the as-received PEKK samples were surfaced and then polished, using a random-orbital sander with the following paper sequence: P120 (for surfacing), P240, P600, P1200, P3000, P6000. Even though the P6000 finishing did produce an apparent mirror-polish (similar to the PMMA surfaces), the full sequence did however not remove all surface imperfections prior to texturing, such that small scratches could still be observed with a microscope. In the present study, the selected abrasive material (Barton HPX garnet) is among the most used in AWJ machining, such as the selected size grades (#220 and #120). SEM images of both abrasive types are shown in Fig. 1. The density and elastic moduli of all the abovementioned materials are given in Table 1.

2.2. Texturing process

Surfaces were prepared using a modified IDE-III AWJ head from H2O JET, 100040–1–F On/Off valve assembly and P–III nozzle body, mounted on a TX2–90XL 6-axis robot from Stäubli (Fig. 2a). High pressure was delivered by a K100 15 kW pump from KAMAT. All other fixed parameters are listed in Table 2. The orifice diameter was chosen relatively small in order to limit water flowrate, and therefore that of abrasive particles. This latter was systematically adjusted to an optimal value, depending on the supplied pump pressure and particle mesh size, using a proprietary model described in [34]. Finally, the stand-off distance (SOD) was set to 200 mm in order to maximize the spread of the particle flow (and therefore, limit overlapping events), as well as minimize some possible influence of the water phase, for it is known to lose energy quickly in the air [35,36].

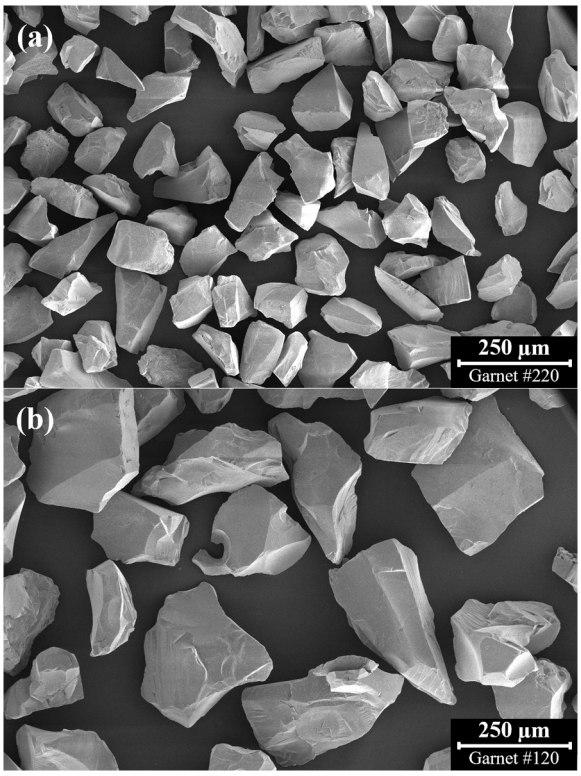

Fig. 1. SEM image of the Barton HPX garnet abrasive for mesh grade (a) #220 and (b) #120.

Table 1
Physical properties of the target-materials and abrasive particles used for this study. Values are taken directly from the manufacturer unless another [reference] is stated.

Physical property *Symbol* (unit)	PMMA	PEKK 7002	HPX Garnet
Absolute density ρ (g/cm^3)	1.19	1.29	4.0
Young's modulus E (GPa)	3.30	3.80	201 [32]
Poisson's ratio ν (-)	0.39	~0.45 [33]	N/A

For the development of the numerical model and to assess its performance, a full factorial design (2^3) of single-pass AWJ treatment was conducted. The tests were performed using various conditions, as indicated in Table 3. Each treatment was repeated three times on the same test-specimen, as schematized in Fig. 2b. The pump pressures, which define the limiting value for the impact velocity of the particles, were selected so as to be representative of the range used for machining fibre reinforced polymers (FRP). In fact, at standard process conditions, maintaining the pressure below 1000 bar ensures the absence of ply delamination in case of unexpected particle flow reduction.

2.3. Methodology used for surface roughness measurement

There is a handful of techniques to measure surface topography. Beyond the initial cost of the equipment, the choice of profilometer is essentially influenced by the required precision and acceptable duration of the measure, as well as the mechanical and optical properties of the target-material. On one hand, contact profilometers are slow and

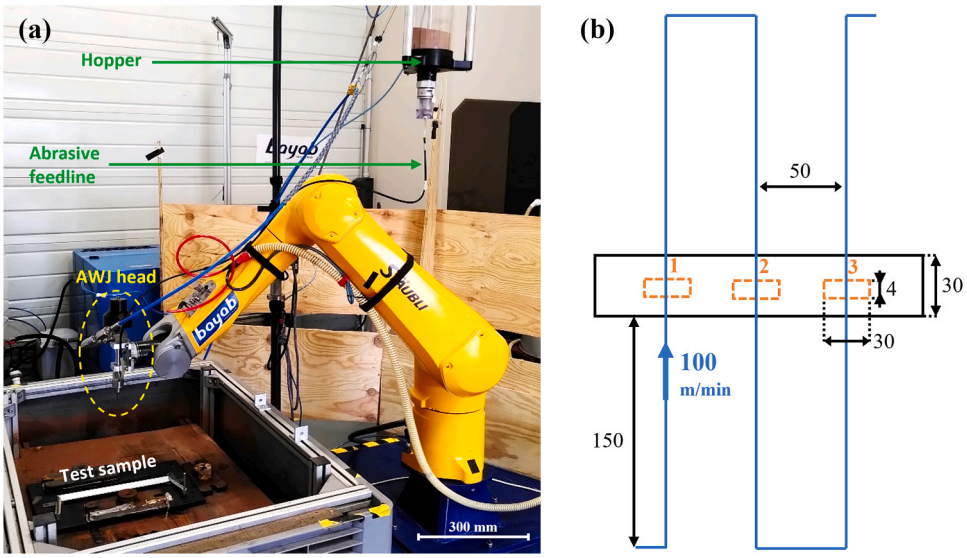

Fig. 2. (a) Photograph of the experimental apparatus used for the texturing process and (b) schematic view of the specimen with the texturing path and dimensions (in mm).

Table 2
Fixed AWJ parameters used in this study.

Parameter	Value
Orifice	P-IV, diamond, Ø0.178 mm
Focusing tube	H2O, Ø0.56 mm, L 50.8 mm
Abrasive feed	PVC, Ø3.8 mm, L∼1200 mm
Abrasive material	Barton HPX crushed garnet
Jet incidence angle	90° (normal to target)
Stand-off distance	200 mm
Tool traverse speed	100 m/min

Table 3
AWJ treatment testing conditions (complete factorial experiment).

Parameter	Low value	High value
Mesh size of particles (mean diameter in μm)	#220 (∼112)	#120 (∼180)
Water pump pressure in bar (limiting velocity in m/s)	400 (283)	1000 (447)
Substrate material ($E/(1-\nu^2)$ in MPa)	PMMA (3900)	PEKK (∼4800)

therefore generally confined to 2D profile measurement. Also, their precision is limited by the size, geometry and wear of the stylus tip, and they can introduce measurement errors on soft materials or damage brittle targets. On the other hand, non-contact light-based solutions are significantly faster, but some of the more advanced technologies such as focus-variation matrix profilometers can have trouble reconstructing highly reflective and/or refractive surfaces. Similarly, the presence of out-of-plane foreign bodies (embedded particles, dust and lint deposits, carbon fibres in composites, etc.) can further diminish measurement accuracy. Therefore, to measure the topography of reflective semi-crystalline polymer surfaces like PMMA and PEKK, the confocal profilometer, with its point-like non-contact scanning probe, is a good compromise between scanning speed and measurement fidelity.

In this study, the surface topography of the textured samples was measured using an Altisurf 520 profilometer from ALTIMET, based on the principle of extended field confocal microscopy with white light. An optical probe, with a Z range of 300 μm and a Z resolution of about 10 nm, was used for all measurements. For each jet pass, an area of 4×30 mm^2 was scanned using a lateral resolution of 3 μm (resulting in a pixel size of 9 μm^2). The measurement conditions (acquisition frequency and probe traverse speed) used for each substrate material are reported in Table 4.

The raw surface maps were post-treated in MATLAB to remove the measurement noise and artefacts. The same operations were applied to all samples so as not to introduce hidden discrepancies in the results. First, as the extracted surfaces appeared with some substantial curvature (Fig. 3a), a 3rd order polynomial shape was fitted and subtracted to the elevation values so as to flatten them below the 10 μm scale. This shape was chosen as an all-encompassing filter, ensuring that any raw surface measured (present and future) would be correctly flattened out. Due to the light-reflective surface of the measured samples, one systematic artefact was observed, whose most prominent feature consisted of a periodic wave pattern with an amplitude lower than 1 μm and a wavelength of about 90 μm (i.e., 30× the probe's scan step). This longitudinal groove pattern (Fig. 3b) was confirmed to be a measurement artefact after varying the direction of scan, which changed the groove direction accordingly. To remove this defect, advantage was taken of the overall low density of topographical objects resulting from particle impacts on the surface, and each longitudinal line of measuring points was independently fitted with a sum of 8 cosine functions. This number was chosen as a compromise in order to match the general curvature of the line, while ignoring steep topographical objects. In addition, the datasets to be fitted were bounded to $\bar{z} \pm 2\sigma_z$ to hinder the influence of high-elevation features on the fitting operation. Finally, the fitted function was subtracted to each initial elevation value. Consequently, the wave pattern was flattened without altering the actual morphological features, although some low-amplitude noise subsisted (Fig. 3c). A thresholding function was therefore applied to remove this residual noise. First, having acknowledged that the density of craters exponentially decreased with distance from the jet's path (Fig. 5), the histogram of elevations was drawn in an area of 4×4 mm^2 on both extremities of the sample (farthest to the left and right of the jet's path), which were assumed to be nearly devoid of craters. As expected from white noise, the plotted data in these regions followed a clear normal distribution (Fig. 4). Then, both datasets were fitted with a gaussian curve, and the

Table 4
Surface measurement conditions for PMMA and PEKK samples.

Parameter	PMMA	PEKK
Acquisition frequency (Hz)	1000	300
Probe traverse speed (mm/s)	3	0.9

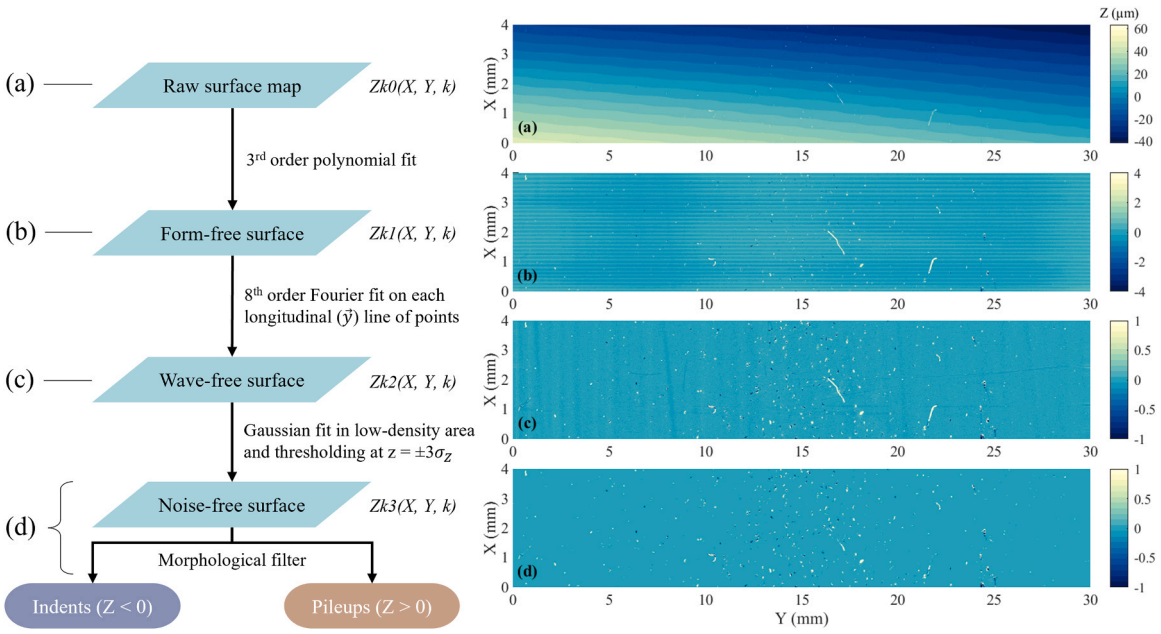

Fig. 3. Post-treatment procedure applied to the acquired surface maps and illustration of the result of each post-processing steps on a PMMA surface treated with #220 particles at a pressure of 400 bar. (a) raw surface map acquired from the profilometer; (b) surface after application of a 3rd order polynomial shape filter; (c) surface after wave artefact removal using a custom algorithm; (d) final surface after noise removal and application of a morphological filter.

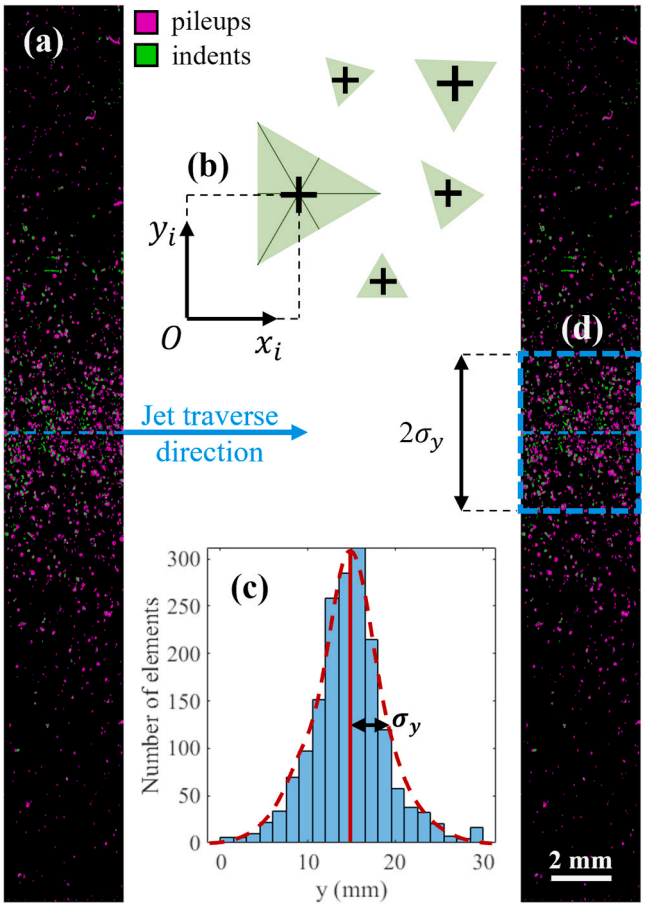

Fig. 5. Procedure for the selection of the measurement area: (a) post-treated 4×30 mm^2 binary surface map with pileups and indents; (b) localization of the centroid for each indent's projected area; (c) plotted histogram of the indents' y ordinates; (d) selection of the measurement area, taken as two standard deviations of the indents' y ordinates, centred at the mean.

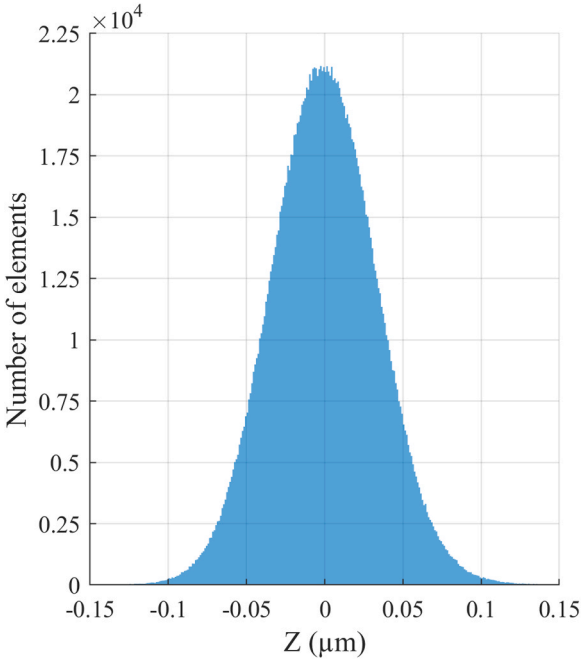

Fig. 4. Histogram of the elevation values around Z = 0 in an area of minimal AWJ treatment density, showing a normal distribution that is typical of white noise (PMMA sample treated with #220 particles at 400 bar).

values $\bar{z}+3\sigma_z$ from both fits were stored. Finally, a linear function linking these thresholds was computed. Extruding the function along the $\vec{x}$ direction returns the threshold matrix Z_{th} such that $\{Z < -Z_{th}$ else $0\}$ corresponds to the elevation of indents and $\{Z > Z_{th}$ else $0\}$ that of pileups (Fig. 3d). Also, in order to remove long and narrow scratches that could still subsist after the previous operations, a morphological filter was applied to target all continuous elements with a minimum Feret diameter (i.e., the smallest dimension that would be measured using a calliper) of less than 2 pixels and a Feret aspect ratio (i.e.,

maximum over minimum) of more than 7.

Lastly, for each post-treated 4×30 mm^2 binary surface map (Fig. 5a), the spatial coordinates of the indents' centroid were collected (Fig. 5b). Since the distribution of the y ordinates (i.e., longitudinal to the sample) was near gaussian (Fig. 5c), a smaller measurement area was selected so that the spatial distribution of craters inside could be considered uniform (Fig. 5d) and, therefore, comparable to the modelled version. For this study, the measurement length was taken as two standard deviations (centred at the mean) of the indents' y centroid ordinates.

The following hypotheses are assumed for the rest of the study:

1. Perfect substrates: even though clear morphological differences between the untreated PEKK and PMMA samples were observed, all surfaces before abrasive treatment will be considered pristine. Therefore, any morphological feature observed after post-treatment will be de facto attributed to the AWJ process, including some residual scratches and embedded particles. Also, it is important to mention that the mechanical parameters of both polymers are different and this, combined with the overlooked deviations in initial roughness, may result in disparate responses to AWJ.
2. Single-phase treatment: any potential effect of the jet's high-velocity water-component on the target's morphology will be ignored.
3. Distinctive outputs: the influence of crater overlapping will be considered negligible for the low impact coverage values resulting from single jet passes with high traverse speed. Any observed continuous topographical object below the initial surface will be assumed to result from one single impact.

3. Numerical model

An original numerical model is proposed, to help determine if the seemingly unpredictable nature of AWJ textures could in fact be reduced to some orderly, physically interpretable patterns. Rather than modelling the indentation mechanisms, experimental topographical data were fed to the model. Coincidentally, this makes the proposed model more versatile, as the entry parameters can be exchanged without impairing its core functionalities. Indeed, it was designed to adapt to new entries without the need for re-identification, such that no arbitrary adjustment parameters were introduced. Also, for the model to be relevant in an industrial context, the number of computing operations was kept to a minimum. Therefore, a semi-analytical approach was chosen, and the interactions between topographical entities were not permitted. Finally, the surface coverage of the generated craters was one of the main control variables of the model.

The coverage of a surface treatment is commonly assumed to be the ratio of modified area to the targeted area (Fig. 6). However, such a visual definition falls short when the impacted areas overlap. Thus, there exist two competing definitions of surface coverage for impact-based processes [26,37]:

- Effective coverage c_e is the proportion of the target-surface that has been indented at least once, and the preferred definition for shot-peening applications. A value of 100 % ("full coverage") corresponds to a modification of all parts of the target surface by the treatment. Because the coverage percentage is visually assessed, values above 100 % are usually estimated through extrapolation based on the duration of treatment needed for full coverage.
- Impact coverage c_i counts all hits on the target as separate entities and can therefore be greater than 100 % even if $c_e < 100$ %. In the absence of overlapping, c_i and c_e are strictly identical.

For a uniform random distribution of impacts, the effective coverage of indents can be mathematically described by Eq. 1, as initially proposed by Kirk & Abyaneh [22]:

$$c_e = 1 - e^{-n_i \bar{a}} \tag{1}$$

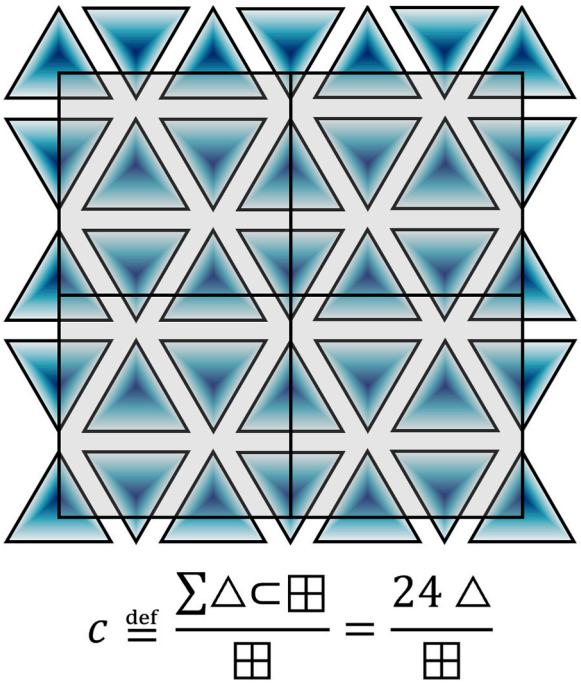

Fig. 6. Definition of surface coverage as the sum of the projected areas of all the indents contained inside some measurement area (here equal to the cumulative area of 24 identical regular triangles) divided by said measurement area.

with n_i the number density of impacts and $\bar{a}$ the average projected area of an indent, whereas the impact coverage is simply expressed by Eq. 2:

$$c_i = n_i \bar{a} \tag{2}$$

As it encompasses more information and is easier to compute, c_i will be the definition of coverage used throughout this study. However, only values below 100 % will be considered. Therefore, from this point on, "$\forall c_i$" is to be understood as "$\forall c_i \leq 100$ %". Similarly, if η is the number of pileups per indent and $\bar{\lambda}$ the average projected area of a pileup entity, the surface coverage of pileups is:

$$\kappa_i = \eta n_i \bar{\lambda} \tag{3}$$

For each textured sample, a parametrization set Γ_i of the generated crater profile can be extracted. It was defined as a m-long set of relevant combinations of each measurable quantity, expressed as in Eq. 4:

$$\Gamma_i = \left\{ \mathscr{C}_m^{14} \left(\underbrace{c_i, \bar{a}, \bar{h}, \bar{V}, \chi_a, \chi_h, \chi_V}_{\text{indents}}, \underbrace{\kappa_i, \bar{\lambda}, \bar{\zeta}, \bar{\Upsilon}, \chi_\lambda, \chi_\zeta, \chi_\Upsilon}_{\text{pileups}} \right) \right\} \tag{4}$$

where:

- $\bar{a}, \bar{h}, \bar{V}$ are respectively the average projected area, depth, and volume of indents,
- $\bar{\lambda}, \bar{\zeta}, \bar{\Upsilon}$ are respectively the average projected area, height, and volume of pileups,
- $\chi_a, \chi_h, \chi_V, \chi_\lambda, \chi_\zeta, \chi_\Upsilon$ are measurements of the dispersion for the quantities in subscript.

Each element of a set Γ_i constitutes an entry parameter for the proposed model. Therefore, the set must be as short and simple as possible, and must satisfy the following property (Eq. 5) regarding the modelled arithmetical mean height S_a^*:

$$S_a^*(\Gamma_i(k)) \approx S_a(k) \quad \forall k \tag{5}$$

where k is the textured sample index.

Ideally, it should also give the best correlation possible for at least one parameter for each of the 13 core morphological functions identified in [17]. In this study, only five areal texture parameters were investigated:

- The first three members of the Core Parameter Set (CPS) from [17], namely the arithmetical mean height (S_a), skewness (S_{sk}) and kurtosis (S_{ku}) of the height distribution,
- One parameter from the V_v (void volume) family, as insighted by the C_v (crater volume) parameter from [14]: the dale void volume (V_{vv}) was chosen as it is also part of the CPS,
- One parameter with an explicit geometric definition: the developed interfacial area ratio (S_{dr}).

Table 5 specifies the core function (CF) represented by each of these parameters (RP), alongside their mathematical expression for a regular XY-grid of N elevation points, as computed in the proposed model.

The simulated indent geometry was selected based on the following criteria:

- low mesh complexity,
- complete surface tiling at $c_i = 100$ %,
- closest geometric proximity to real indents.

Based on the experimental investigation, the circularity of an average indent was about 0.45. The closest regular 2D polygon is the triangle with a value of 0.61. For the sake of simplicity, indents were therefore modelled as tetrahedra with regular bases. This is consistent with the relatively frequent observation (about 1 in 10) of "Berkovich"-type structures (Fig. 7).

The modelled surfaces were constructed so as to mimic what a scanning probe profilometer would measure (Fig. 8). Firstly, the triangular faces of all 72 tetrahedral indents were drawn according to the user-specified dimensions and coverage. Secondly, an area of interest (or measuring cell) comprising exactly 32 indents was defined to reflect all the introduced morphological features in an isotropic and unbiased manner. A regular XY-grid of points was created inside the measuring cell according to the user-specified lateral resolution. Finally, a ray/triangle intersection algorithm [38] was used to project the grid of points onto the tetrahedral mesh, based on the method described in [39]. Fig. 9 shows the surface maps resulting from the numerical model for varying coverage values.

Using the proposed model, it was possible to try and determine which configuration of the parametrization set $\{\Gamma_i\}$ would satisfy Eq. 5. Thus, the post-treated AWJ-textured samples were analysed to extract all the quantities that appear in Eq. 4, as well as the relevant areal field parameters. Next, different combinations of these geometric quantities were fed to the model, and the same parameters were computed for the modelled version, up until a satisfying parametrization set was identified (Fig. 10).

Hereinafter, when a statement concerns modelled indents that are strictly identical regarding any dimension, it will be indicated by the use of a and/or h in place of their arithmetical means $\overline{a}$ and $\overline{h}$, unless these are necessary for rigorous generalization or emphasis.

Table 5
Mathematical expression computed for all the areal texture parameters used in this study, with N the number of pixels in the elevation matrix $Z(x,y)$. The notation $\{*\}^{\searrow}$ indicates sortation in descending order.

CF	RP	Discrete mathematical definition
I	S_a	$\frac{1}{N}\sum_{k=1}^{N}\lvert Z_k-\overline{Z}\rvert$
II	S_{sk}	$\sqrt{N}\left(\sum_{k=1}^{N}(Z_k-\overline{Z})^2\right)^{-\frac{3}{2}}\sum_{i=1}^{N}(Z_k-\overline{Z})^3$
III	S_{ku}	$N\left(\sum_{k=1}^{N}(Z_k-\overline{Z})^2\right)^{-2}\sum_{k=1}^{N}(Z_k-\overline{Z})^4$
X	V_{vv}	$\frac{1}{N}\sum_{k=0.8N}^{N}\lvert\{Z-\overline{Z}\}_k^{\searrow}-\{Z-\overline{Z}\}_{0.8N}^{\searrow}\rvert$
XII	S_{dr}	$\frac{1}{N}\sum_{k=1}^{N}\left(\sqrt{1+\left\lvert\frac{\partial Z}{\partial x}\right\rvert_k^2+\left\lvert\frac{\partial Z}{\partial y}\right\rvert_k^2}-1\right)$

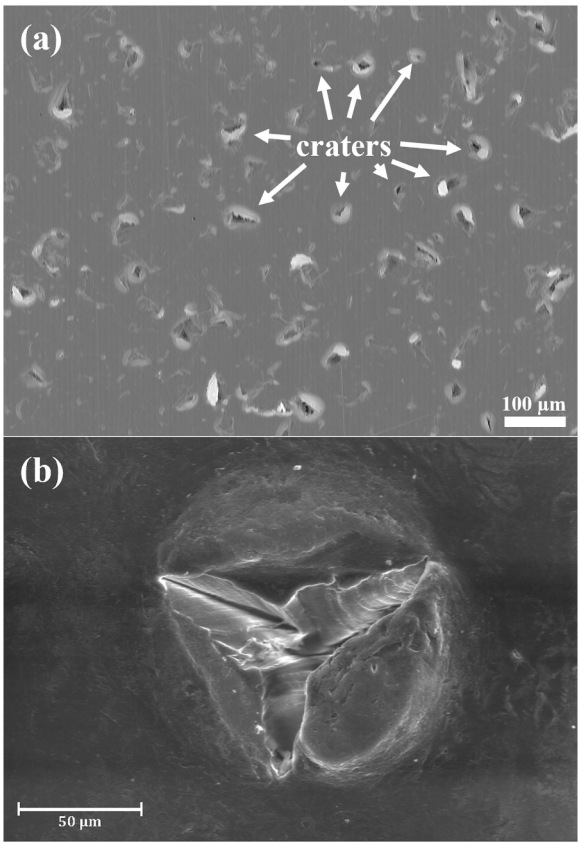

Fig. 7. PEKK surface blasted by AWJ: (a) altitude grey map showing matter above the initial plane piling up around polyhedral indents; (b) SEM image of a "Berkovich"-type crater.

4. Results & discussion

4.1. Topographical parameter behaviour

Prior to experimental investigation with AWJ-textured samples, a theoretical analysis was performed in order to assess the general validity of the model and explore its parametric behaviour. It has been useful to remark that some field parameters have simple analytical expressions, provided an equally simple modelled configuration. For instance, the developed interfacial area ratio (S_{dr}) is a hybrid parameter having a direct physical meaning. It is expressed as the ratio of the surface area contributed by the topographical micro-features to the planar definition area [40]. For a homogenous repartition of identical tetrahedral indents, it can be analytically expressed, $\forall c_i$, by Eq. 6:

$$S_{dr} = \left(\sqrt{1+\frac{3\sqrt{3}\,h^2}{a}}-1\right)c_i \tag{6}$$

Eq. 6 can be used as a checksum for the numerical model, in which S_{dr} has a different mathematical expression (Table 5). As expected, a linear evolution of S_{dr} as a function of the surface coverage of indents c_i can be observed in Fig. 11. The slope of the curve (0.00492 on average, considering $h = 1$ µm, $a = 500$ µm^2 and a lateral resolution of 0.25 µm)

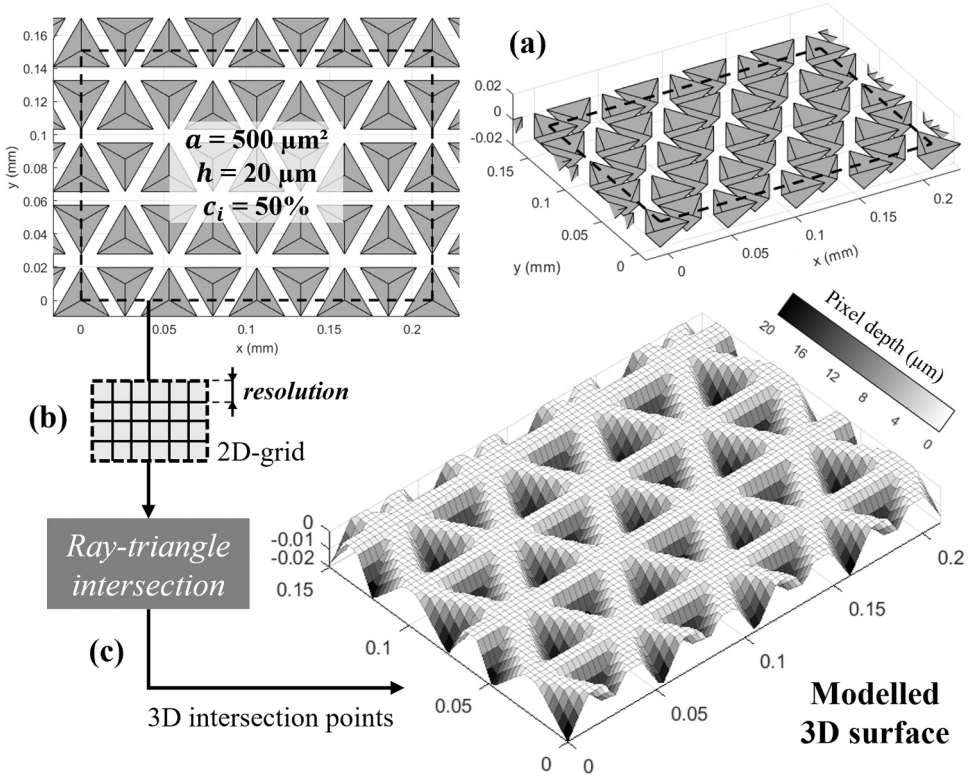

Fig. 8. Three-step process for generating numerical homogenous impact-based surface textures: (a) creation of the triangular faces of the numerical tetrahedral indents according to the user-specified dimensions and coverage; (b) generation of a regular XY-grid of points inside a measuring cell of exactly 32 craters; (c) intersection of vertical rays originating from said points with the triangular mesh of indents.

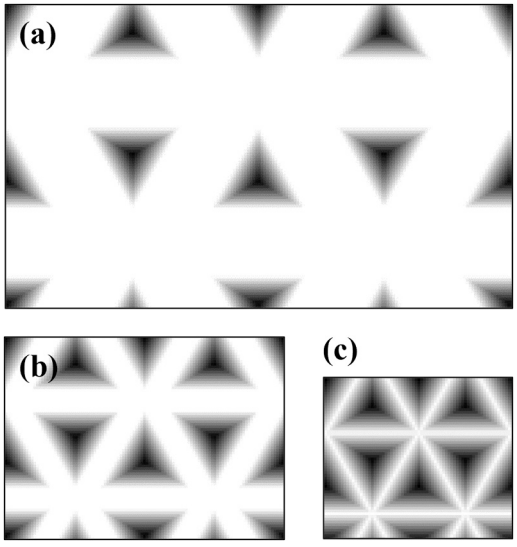

Fig. 9. Grey surface map of a modelled surface with eight indents for a coverage of (a) 20 %, (b) 50 % and (c) 100 % (darker areas correspond to higher depth below the initial plane, and the map's scale was omitted for generalization purposes).

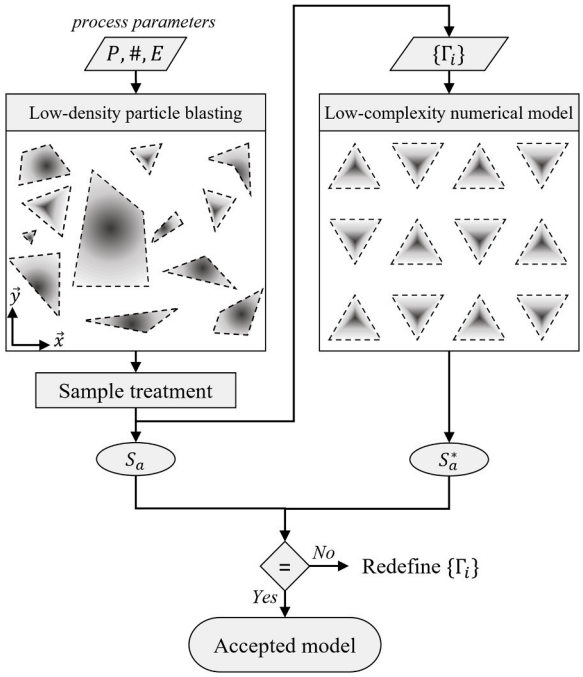

Fig. 10. Operational diagram of this study.

is close to the theoretical value (0.00518) computed using Eq. 6. However, this correlation is heavily dependent on the resolution of the model. In fact, the modelled S_{dr} converges to the analytical value as the pixels get smaller. Such a correlation attests that the numerical model is free from any major structural defect.

Moreover, being gradient based (Table 5), S_{dr} has the interesting property of additivity. Consequently, an elevation matrix Z, split into points above and below some horizontal plane of altitude z_0, must satisfy Eq. 7:

$$S_{dr}(Z) = S_{dr}(Z \leq z_0) + S_{dr}(Z > z_0) \tag{7}$$

Using this property, it was possible to model the experimental

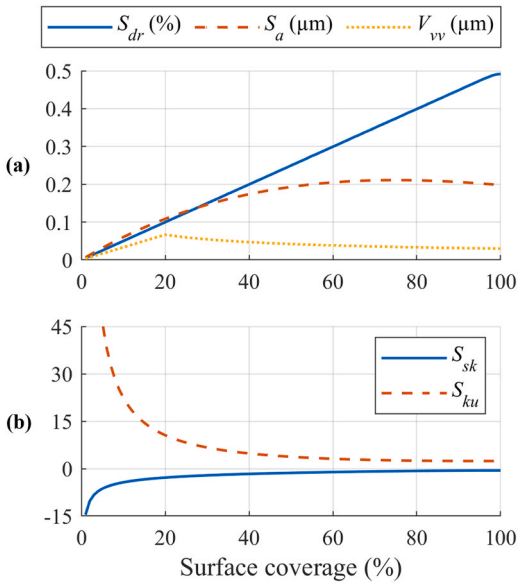

Fig. 11. Effect of the surface coverage (c_i) on surface roughness parameters calculated using the numerical model for a homogenous repartition of identical tetrahedral indents (with $a = 500$ µm^2, $h = 1$ µm, and a lateral resolution of 0.25 µm): (a) arithmetical mean height (S_a), developed interfacial area ratio (S_{dr}) and dale void volume (V_{vv}); (b) skewness (S_{sk}) and kurtosis (S_{ku}).

textures by summing the results obtained from modelling half-surfaces only, thus extending the range of coverages that would not cause overlapping.

Another especially interesting parameter for the purpose of this study was arithmetical mean height (S_a), as it is the most frequently used amongst all areal roughness parameters [14]. In addition, it can be observed from Fig. 11 that S_a is not monotonic with coverage like S_{sk} and S_{ku}. Yet, contrary to V_{vv}, it remains differentiable on its entire domain of definition. Besides, at a surface coverage of less than 20 %, the behaviours of S_a and V_{vv} were very similar. Finally, it is known that S_{sk} and S_{ku} are parameters of order 3 and 4 respectively (Table 5), meaning that they are very sensitive to both noise and prominent topographical features. For all these reasons and for the sake of intelligibility, the study will be mainly focused on S_a and S_{dr} hereafter.

Despite the complex behaviour of S_a with coverage, a linear relationship of S_a as a function of average depth $\bar{h}$ was observed for any value of the surface coverage of indents c_i (Fig. 12). Therefore, it can be

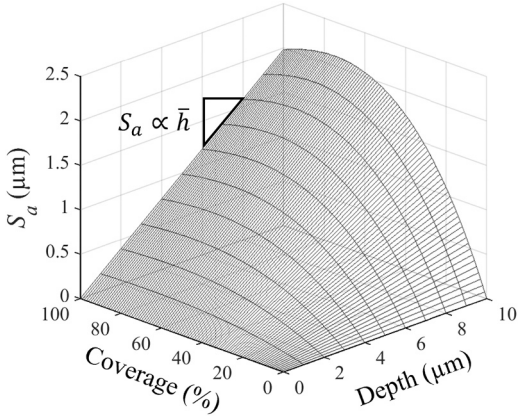

Fig. 12. 3D graph showing the influence of surface coverage (c_i) and average indentation depth ($\bar{h}$) on arithmetical mean height (S_a) for a homogenous repartition of identical tetrahedral indents with a constant regular base of area $a = 500$ µm^2.

relevant to introduce the volume coverage of indents w_i, as well as that of pileups ω_i:

$$\begin{cases} w_i = c_i \bar{h} \\ \omega_i = \kappa_i \bar{\zeta} \end{cases} \tag{8}$$

Besides, an independence of S_a with average projected area $\bar{a}$ could be observed as long as c_i is conserved, indicating scale-invariance of S_a along the XY-plane. However, by introducing some variability in the dimensions of indents, complex behavioural changes were highlighted by the model.

Looking at topographical data from real AWJ-textured samples (Fig. 13), it can be observed that the distributions of indent depths, projected areas and volumes are all positively skewed, so that approximately ¾ of craters have a maximal depth lower than the distribution's mean. This observation was reproduced for all the measured geometric quantities and textured samples, as shown in Table 6. To consider this dichotomy in crater geometry while considerably limiting the complexity of the numerical model, the modelled surface was modified to be composed of ¾ of "small" indents and ¼ of "big" ones (Fig. 14). The parameters χ_a and χ_h were introduced, so that:

$$\chi_a = a_B / a_S \tag{9}$$

where a_B and a_S are the projected areas of "big" and "small" craters, respectively (idem for h).

The mean value was of course preserved, such that:

$$a_B + 3a_S = 4\bar{a} \tag{10}$$

Therefore, the projected areas relative to "big" and "small" indents, as computed in the model, were:

$$\begin{cases} a_B = \dfrac{4\chi_a}{\chi_a + 3}\bar{a} \\ a_S = \dfrac{4}{\chi_a + 3}\bar{a} \end{cases} \tag{11}$$

As shown in Fig. 15, it was found that:

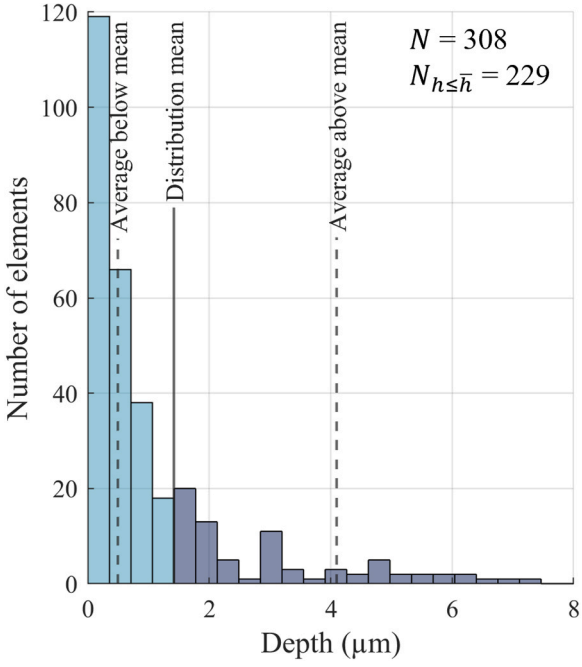

Fig. 13. Example of statistical distribution for the maximal depths of indents, where about three quarters of the total number of indents have a maximal depth below the arithmetical mean of the entire distribution (PMMA sample treated with #120 particles at 400 bar).

Table 6
Proportion (in %) of values below the arithmetical mean for all the measured geometric parameters (columns) and each textured sample (lines).

Proportion of values below distribution mean for each sample (%)	a	h	V	λ	ζ	Υ
	79	81	85	78	75	83
	68	67	75	75	73	81
	77	69	77	78	74	82
	70	63	74	84	80	89
	68	67	72	69	69	77
	68	71	76	90	77	92
	77	78	81	74	72	80
	75	74	79	73	71	77
	65	67	73	73	70	78
	69	73	77	68	68	74
	62	46	69	63	61	68
	73	67	79	63	68	73
	77	79	86	81	78	87
	77	78	85	80	77	86
	73	76	82	78	77	84
	70	73	82	75	74	82
	73	80	81	78	78	87
	70	75	80	74	75	85
	72	76	86	74	77	85
	68	72	76	74	74	81
	72	76	81	75	75	82
	70	72	77	74	71	80
	69	70	78	69	78	82
	69	75	80	69	70	76
	66	72	76	68	73	78
	65	67	75	71	72	81
Mean	**71**	**72**	**79**	**74**	**73**	**81**

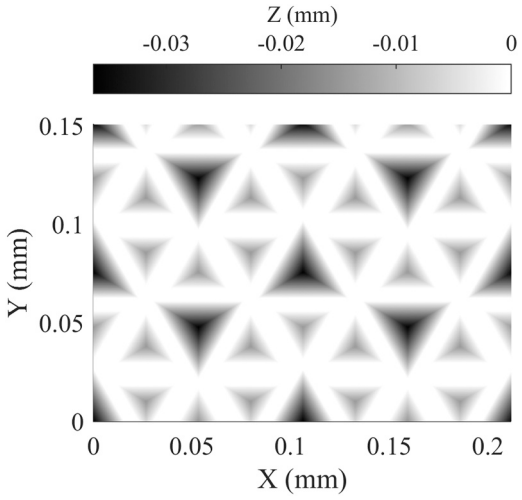

Fig. 14. Generated surface with ¼ of the indents having both a projected area and depth 2.5 times higher ($\chi_a = \chi_h = 2.5$) than the other ¾, with $c_i = 50$ % and $\overline{h} = 20$ µm.

- Area variation alone did not change the evolution of $S_a(c_i, \overline{h})$, as long as there was no overlapping of indents (which the model cannot yet process).
- Depth variation alone increased S_a at high impact coverage. It is interesting to note that:

$$\lim_{\chi_h \to \infty} (S_a(c_i, \overline{h}, \chi_h)) = S_a\left(\frac{1}{4}c_i, 4\overline{h}\right) \tag{12}$$

- Considering both depth and area variations together, the initial slope of $S_a(c_i, \overline{h})$ was systematically increased by a factor $X(\chi_a\chi_h)$. It is possible to show analytically that:

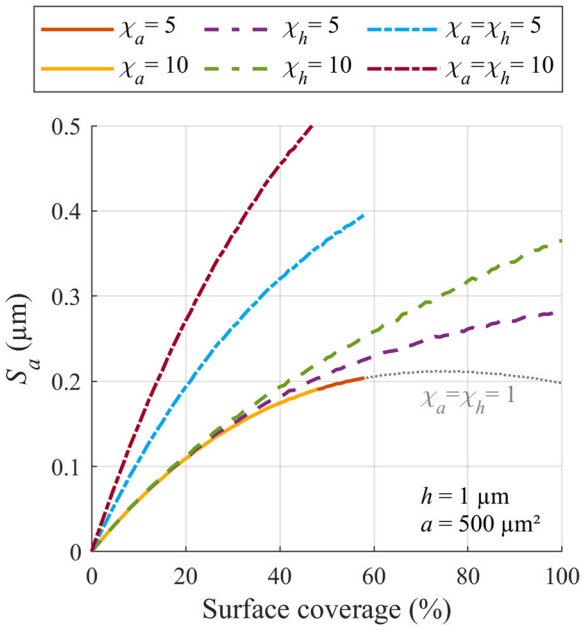

Fig. 15. Effect of indent size variation parameter χ on $S_a(c_i)$, for a constant average indentation depth $\overline{h}$ of 1 µm. Values resulting from overlapping geometries were removed from the graph.

$$X = \frac{4(\chi_a\chi_h + 3)}{(\chi_a + 3)(\chi_h + 3)} \tag{13}$$

4.2. Application to AWJ-textured samples

Knowing how the entry parameters of the model affect the resulting roughness parameters, it was possible to assess its performance in modelling the complex textures generated by AWJ treatment. For this, all the geometric and numerary quantities introduced in Section 4.1 were measured. The quantity χ_q was measured as the ratio of the average value above the mean of a distribution q to the average value below the mean (as previously highlighted in Fig. 13). For example, the depth h of indents was expressed as in Eq. 14:

$$\chi_h = \frac{\overline{h_{h>0}}}{\overline{h_{h\leq 0}}} \tag{14}$$

Overall, for a given substrate, larger and deeper craters were observed with increasing particle size and pump pressure, as shown in Fig. 16. However, the factors influencing the number density of the different crater entities appeared much more complex and were not considered in this study.

Also, the influence of the measurement noise on roughness parameters was difficult to model, as it did not appear to be linked to any measurable quantity. Looking at the measured arithmetical mean height (S_a) values with and without noise, no clear relationship between the two functions could be established (Fig. 17). Besides, explicit differences in the behaviour of noise with S_a between the two materials were highlighted. In fact, it is important to mention that the threshold values for the removal of noise from the measured point clouds (as described in 2.3) were 3 to 7 times greater for PEKK samples (0.66 µm on average) than for PMMA (0.15 µm). Consequently, the S_a measured for PEKK samples were much more impacted by noise suppression.

Besides this numerical noise of low amplitude (less than 1 µm), there was significant heterogeneity in the residual morphological features, with very distinct features above and below the zero-elevation plane, which limited the relevancy and repeatability of the analysis. On the lower side, long, narrow grooves were often present due to excessive

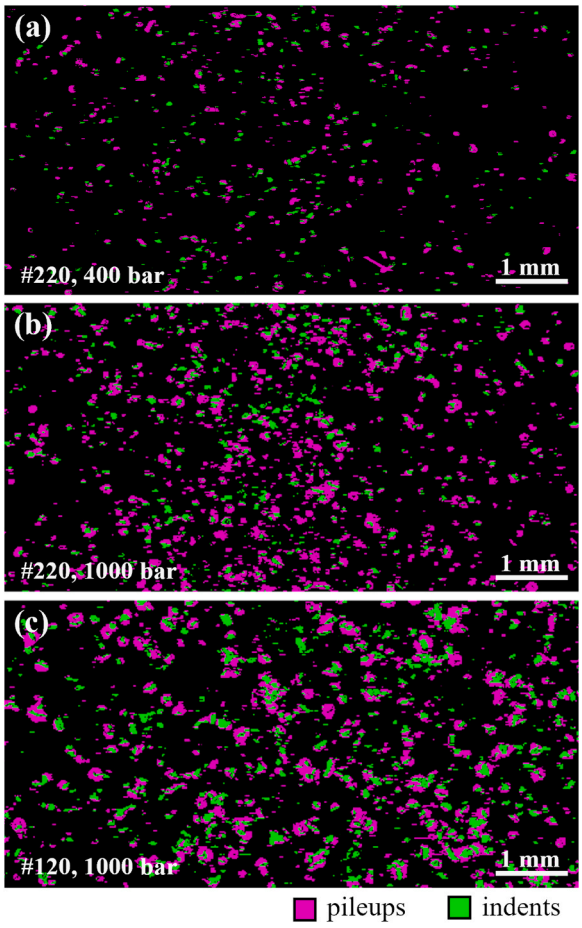

Fig. 16. Examples of binary surface maps after post-treatment, showing the projected areas of pileups and indents for PMMA samples textured with various AWJ conditions: (a) #220 particles at a pressure of 400 bar; (b) #220 particles at a pressure of 1000 bar; (c) #120 particles at a pressure of 1000 bar.

manipulation of the samples. In fact, wiping of AWJ-textured samples with cloth is likely to set loose weakly embedded particles and drag them along the surface, causing prominent scratches to appear. On the upper side, besides the actual pileups associated with aforementioned scratches, dust particles (contamination), permanently embedded abrasive particles, and cloth residue could be observed. Among this list of parasitic features, those that corresponded to the criteria of size and elongation mentioned in Section 2.3 were removed via the morphological filter. However, this operation would likely become ineffective in the case of high surface noise (as with the PEKK samples used in this study) due to the raised probability of overlapping entities. In any case, surface pollution can be considerably reduced by cleaning the textured samples in an ultrasonic bath prior to measurement.

4.3. Modelling of half surfaces

As explained in Section 3, a parametrization set consists of different combinations of the geometric and numerary parameters measured on the experimental samples. The simplest set that can be made is:

$$\Gamma_1 = \{c_i, a, h, \kappa_i, \lambda, \zeta\} \tag{15}$$

Adding variation upon the projected areas and heights yields a second set:

$$\Gamma_2 = \{c_i, a, \chi_a, h, \chi_h, \kappa_i, \lambda, \chi_\lambda, \zeta, \chi_\zeta\} \tag{16}$$

Given that the model was composed solely of tetrahedra, the volume of an entity was necessarily determined by its height and projected area,

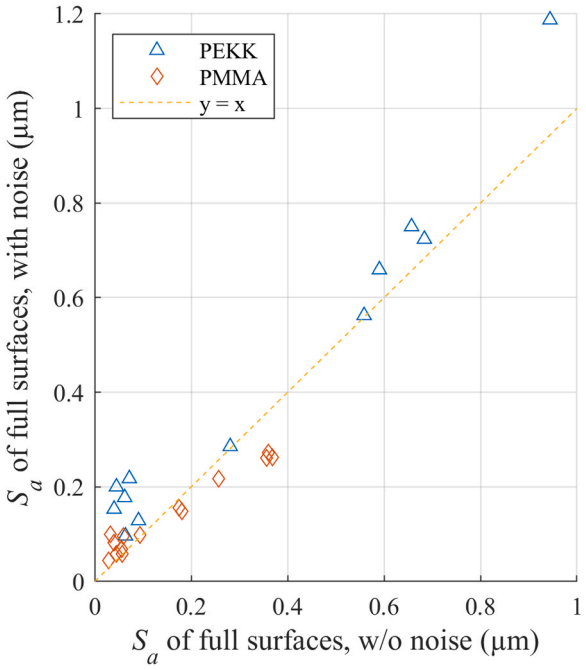

Fig. 17. Concordance between the measured arithmetical mean height (S_a) of all full surfaces (indents and pileups), with (y-axis) and without (x-axis) the measurement noise.

given as entry parameters. However, the actual volume of an indent or pileup can diverge significantly from that of a tetrahedron. To account for this particularity, volume-derived dimensions were introduced in the model. For each of the geometric parameters of the model, they were defined as the value that they would have for a tetrahedron of identical volume, and expressed as in Eq. 17:

$$\begin{cases} A = \dfrac{3V}{h} \\ H = \dfrac{3V}{a} \\ \Lambda = \dfrac{3\Upsilon}{\zeta} \\ \mathrm{Z} = \dfrac{3\Upsilon}{\lambda} \end{cases} \tag{17}$$

Thus, sets Γ_3 and Γ_4 are respectively equivalent to sets Γ_1 and Γ_2, but with the areas and heights changed to the volume-derived definitions from Eq. 17, leading to:

$$\begin{cases} \Gamma_3 = \{c_i, A, H, \quad \kappa_i, \Lambda, \mathrm{Z}\} \\ \Gamma_4 = \{c_i, A, \chi_A, H, \chi_H, \kappa_i, \Lambda, \chi_\Lambda, \mathrm{Z}, \chi_\mathrm{Z}\} \end{cases} \tag{18}$$

Finally, a fifth set was introduced, based on set Γ_4 with the dispersion parameter χ_A removed:

$$\Gamma_5 = \{c_i, A, H, \chi_H, \kappa_i, \Lambda, \mathrm{Z}, \chi_\mathrm{Z}\} \tag{19}$$

For each parametrization set, the performance of the model was quantified using the concordance correlation coefficient (Table 7), which was computed using Eq. 20:

$$\rho_c(u, v) = \frac{2\sigma_{uv}}{\sigma_u^2 + \sigma_v^2 + (\bar{u} - \bar{v})^2} \tag{20}$$

where σ_{uv} is the covariance of the data samples u and v.

This criterion was chosen as it reflects the proximity of the data to the $y = x$ line, as opposed to the coefficient of determination (R^2), which has a more frequent usage but only considers closeness to a linear relationship.

Overall, set Γ_5 gave the most accurate results. According to the

Table 7
Concordance correlation coefficient ρ_c calculated for each topographical parameter and each parametrization set.

	Set	Γ_1	Γ_2	Γ_3	Γ_4	Γ_5
Indents (Z < 0)	S_a	0.541	0.947	0.961	0.729	0.961
	S_{sk}	0.814	0.823	0.813	0.832	0.847
	S_{ku}	0.754	0.727	0.752	0.758	0.745
	V_{vv}	0.544	0.949	0.961	0.733	0.961
	S_{dr}	0.246	0.704	0.724	0.946	0.940
	Mean	**0.580**	**0.830**	**0.842**	**0.800**	**0.891**
Pileups (Z > 0)	S_a	0.539	0.948	0.961	0.833	0.961
	S_{sk}	0.331	0.380	0.331	0.399	0.480
	S_{ku}	0.141	0.165	0.141	0.170	0.217
	V_{vv}	0.545	0.948	0.961	0.840	0.961
	S_{dr}	0.266	0.518	0.705	0.807	0.798
	Mean	**0.364**	**0.592**	**0.620**	**0.610**	**0.684**

guidelines for the interpretation of the concordance coefficient [41], there was an almost perfect agreement between the modelled and measured data for both S_a and V_{vv}, with a maximal relative deviation of 4 %. Similarly, a highly substantial agreement was found for S_{dr}, with an error of 20 %. However, the low-complexity numerical model fell short with the shape parameters S_{sk} and S_{ku}, which none of the tested parametrization sets matched confidently, given that they are very sensitive to noise and extrema. An exacerbated divergence was observed for pileups, for which the half-surfaces generally have higher coverage values than those of indents. The concordance between the measured and modelled S_a for the upper half-surfaces is shown in Fig. 18, as well as the relevance of volume coverage (Eq. 8) as a possible independent variable for low-coverage treatments.

4.4. Modelling of whole surfaces

Based on the additivity of the S_{dr} function (Eq. 7), it can be verified that the sum of the modelled S_{dr} values for pileups and indents is indeed equal to the measured S_{dr} of the entire surface (with noise removed) with the fifth parametrization set. As expected, a deviation from the $y = x$ line was observed with increasing S_{dr} values (Fig. 19), with a concordance coefficient of 82.3 %, close to the average of those obtained for each individual half-surfaces (84.5 %). Therefore, the accuracy of the S_{dr} summation technique appeared only limited by the accuracy of the model with each individual half-surface.

To model S_a over the entire surface (indents and pileups), a first modelling strategy, consisting of mixing pileups and indents uniformly

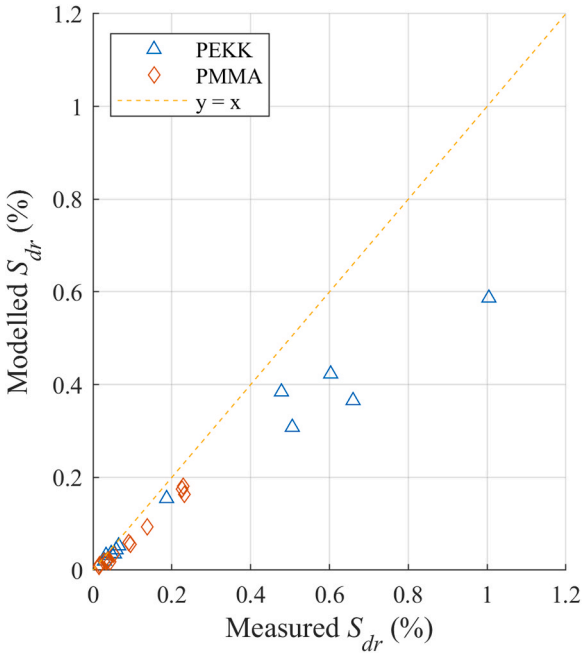

Fig. 19. Concordance between the measured S_{dr} of the full surface (indents and pileups, without noise) and the sum of the modelled S_{dr} of each half-surface using Γ_5.

while preserving a mesh of 32 entities, could be tried (Fig. 20). Consequently, the surface coverage to be computed ("crater coverage") would be the sum of both indents and pileups independent coverages, as expressed in Eq. 21:

$$c_c = c_i + \kappa_i \tag{21}$$

With a concordance coefficient of 93.6 %, this simple strategy did in fact produce a good approximation of S_a for the experimental samples. However, the model slightly underestimated the actual measured value, especially with PMMA samples for which a divergence to the $y = x$ line was clearly visible (Fig. 21a). Thus, the uniform mixing strategy might well be insufficient to properly model AWJ-textured surfaces. Yet, considering also the deviation of S_{dr} with increasing coverage, one could argue that the parametrization set Γ_5 was too simple to capture the full essence of the experimental surfaces. A pragmatic and conservative

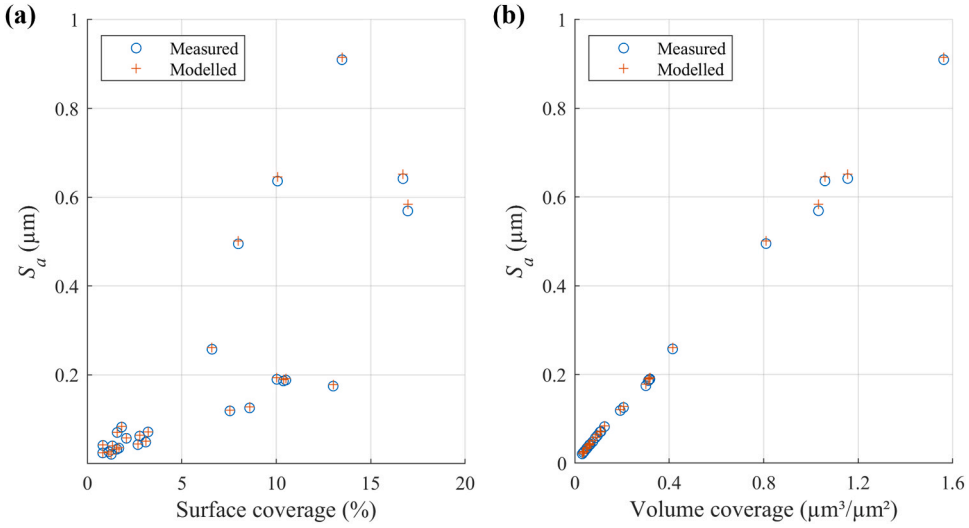

Fig. 18. Evolution of the measured and modelled arithmetical mean height (S_a) as a function of (a) the surface coverage and (b) the volume coverage of pileups with parametrization set Γ_5.

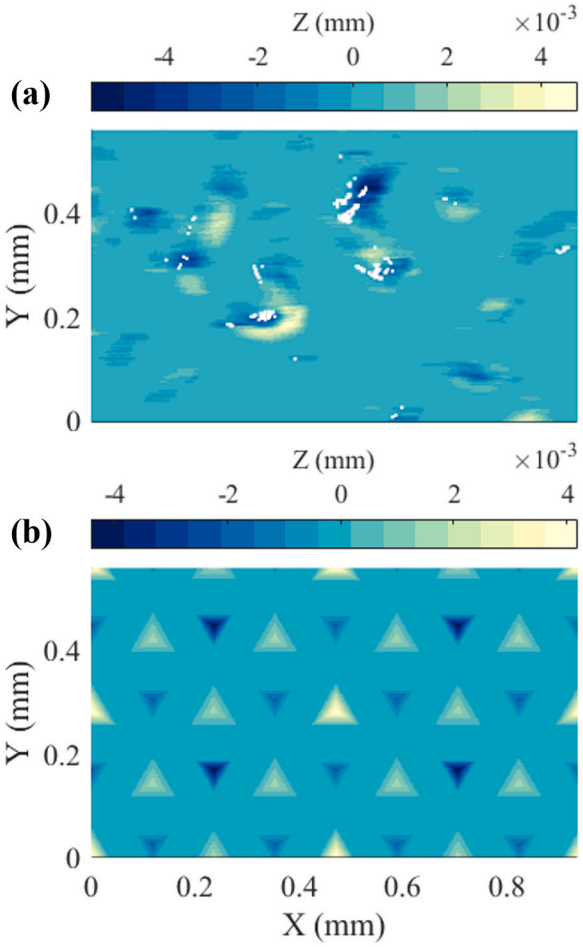

Fig. 20. (a) surface map from a PMMA sample treated with #220 particles at 1000 bar and (b) modelled equivalent full surface (indents and pileups, without noise), using the uniform mixing strategy.

approach for improving the model would be to add a third size bin (category) for both the indents and pileups, such that the equivalent full surface would be comprised of six different geometries instead of four. Theoretically, the more bins added, the closer the equivalent surface should get to its experimental counterpart, and so the smallest number of bins that satisfy the performance criteria should be used. Likewise, an appreciable improvement could involve deviating the base element from a tetrahedron, through the introduction of some measurable "deformation" parameter. Finally, considering the mean S_a and associated range for each AWJ configuration (Fig. 21b), it is clear that PEKK samples were more subject to statistical dispersion compared to PMMA samples, which could partly be due to the lower quality of the surfaces before texturing (initial state). Hence, the application of the presented characterization method to other target-materials would be highly valuable to further assess the performance of the proposed model.

5. Conclusions

The aim of this study was to develop a numerical model capable of accurately predicting key surface roughness parameters resulting from a random impact-based surface treatment process, such as AWJ texturing. The proposed model featured equally spaced tetrahedra with pilotable surface coverage and dimensions. Experimental investigation was conducted on polymer samples textured using the AWJ process and a custom post-treatment algorithm was implemented to extract relevant morphological properties from the point clouds supplied by the profilometer. To validate the model's predictive capabilities, the roughness of a representative uniform mix of indents and pileups was calculated and compared to the corresponding measurements for textured surfaces. Based on these experimental and numerical investigations, the following conclusions could be established:

- It was found that impact-based surfaces could not simply be reduced to a single average indent geometry, as varying heights and projected areas for fixed average values considerably changed the behaviour of areal field parameters as a function of the surface coverage of indents.
- When applied to the proposed model, the parametrization set Γ_5, which featured surface coverage, volume-derived (V-) projected area, V-height, and V-height variation, was shown to agree the most with the experimental S_a, V_{vv} and S_{dr} of half-surfaces.
- The modelling of the S_{dr} of full surfaces with the summation strategy produced an acceptable concordance coefficient of 82 %. However, the consistent deviation to the experimental data observed with increasing coverage suggests that a different parametrization set could better describe this parameter.

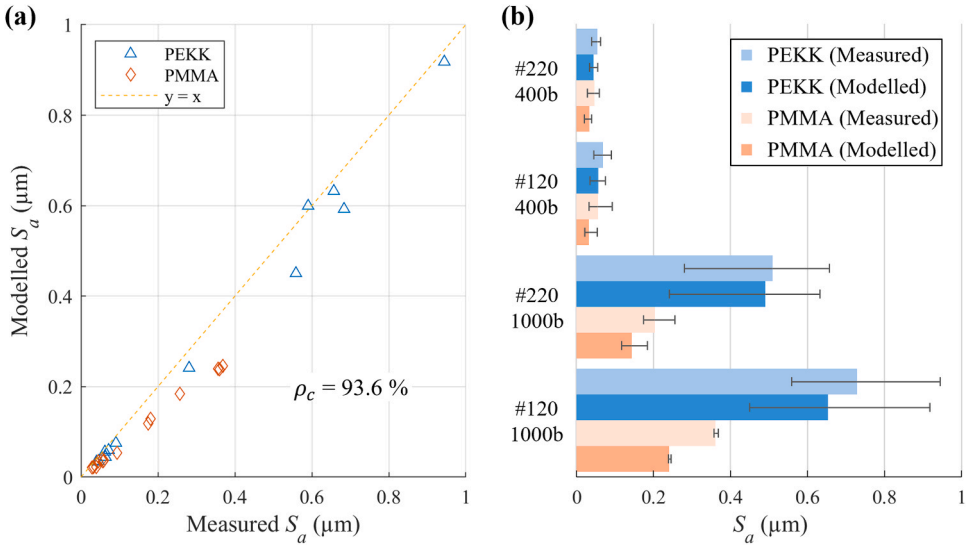

Fig. 21. Concordance between the measured and modelled S_a of the full surfaces (indents and pileups, without noise) for both materials using the uniform mixing strategy, with: (a) $y = x$ comparison of all datapoints and (b) mean value and dispersion (range) for each AWJ configuration (particle mesh size and pressure).

- The prediction of S_a with the uniform mixing strategy exhibited excellent concordance (94 %) with the experimental values, demonstrating the model's reliability in predicting the areal surface roughness of AWJ treatments at low surface coverage (less than 21 %) using common process parameters.
- A significant influence of the target-material on topographic parameters was observed. In fact, textured surfaces made of PEKK were characterized by around twice the roughness of their PMMA counterparts. This variation could be attributed to the difference in initial surface quality between the two polymers, as the measured values of crater coverage were overall higher on PEKK for the same texturing conditions.

The proposed model offers a promising tool for optimizing surface treatment processes and achieving desired surface characteristics. By accurately predicting the resulting roughness parameters, the model can guide the selection of appropriate process parameters, minimizing the need for time-consuming and costly trial-and-error approaches. Furthermore, the model's simplicity and versatility allow for its potential adaptation to other impact-based surface treatment processes, expanding its applicability beyond the AWJ texturing technique explored in this study. However, further work would be needed to assess the viability of the model above the studied range of surface coverage values, which would likely require the implementation of an overlap management solution. Such a tool could eventually be applied to the surface preparation of composite materials for structural bonding, as part of the value chain to optimize the adhesive performance and long-term durability of composite and hybrid (e.g., titanium/composite) structures.

CRediT authorship contribution statement

Pierre Fréquelin: Writing – original draft, Visualization, Software, Resources, Project administration, Methodology, Investigation, Formal analysis, Data curation, Conceptualization. **Agathe Jaillon:** Writing – review & editing, Supervision, Resources, Methodology, Conceptualization. **Sabine Le Roux:** Writing – review & editing, Investigation. **Julien Jumel:** Writing – review & editing, Supervision. **Rédouane Zitoune:** Writing – review & editing, Supervision, Resources, Conceptualization. **François Cénac:** Supervision, Resources, Methodology, Conceptualization.

Declaration of Competing Interest

The authors declare that they have no known competing financial interests or personal relationships that could have appeared to influence the work reported in this paper.

Data availability

Data will be made available on request.

Acknowledgements

The financial and technical support of BAYAB Industries, as part of a broader doctoral work with a grant from the French National Association for Research and Technology (ANRT, grant number 2021/0661), is gratefully acknowledged. The authors would also like to thank Mehdi Salem for kindly providing the SEM images shown in Fig. 1. For the purpose of Open Access, a CC-BY public copyright licence has been applied by the authors to the present document and will be applied to all subsequent versions up to the Author Accepted Manuscript arising from this submission.

Appendix A. – Evolution of the average slope of the modelled $S_{dr}(c_i)$ function with lateral resolution (considering $h = 1$ µm and $a = 500$ µm^2), showing that the model converges towards the analytical value by lowering (improving) the resolution

Resolution (µm)	0	0.25	1	3
$\partial S_{dr}/\partial c_i \times 10^3$	518	492	420	255

Appendix B. – Proof of the expression for the factor X on the slope of the $S_a(c_i)$ curve with a configuration of ¼ of "big" craters, based on volume equilibrium, as S_a is confounded with the total volume of indents when $c_i \to 0$

$$4\overline{a}\overline{h}X = a_B h_B + 3a_S h_S = \frac{4\chi_a \overline{a}}{\chi_a + 3}\frac{4\chi_h \overline{h}}{\chi_h + 3} + 3\frac{4\overline{a}}{\chi_a + 3}\frac{4\overline{h}}{\chi_h + 3} = 4\overline{a}\overline{h}\frac{4(\chi_a\chi_h + 3)}{(\chi_a + 3)(\chi_h + 3)} \tag{B.1}$$

References

[1] Chan KS, Koike M, Mason RL, Okabe T. Fatigue life of titanium alloys fabricated by additive layer manufacturing techniques for dental implants. Met Mater Trans A 2013;44:1010–22. https://doi.org/10.1007/s11661-012-1470-4.
[2] Itoga H, Tokaji K, Nakajima M. H.-N. Ko, Effect of surface roughness on step-wise *S–N* characteristics in high strength steel. Int J Fatigue 2003;25:379–85. https://doi.org/10.1016/S0142-1123(02)00166-4.
[3] Zhu X, Dong Z, Zhang Y, Cheng Z. Fatigue life prediction of machined specimens with the consideration of surface roughness. Materials 2021;14:5420. https://doi.org/10.3390/ma14185420.
[4] Sanaei N, Fatemi A. Analysis of the effect of surface roughness on fatigue performance of powder bed fusion additive manufactured metals. Theor Appl Fract Mech 2020;108:102638. https://doi.org/10.1016/j.tafmec.2020.102638.
[5] Zhao B, Song J, Xie L, Hu Z, Chen J. Surface roughness effect on fatigue strength of aluminum alloy using revised stress field intensity approach. Sci Rep 2021;11:19279. https://doi.org/10.1038/s41598-021-98858-0.
[6] Li W, Li DY. Influence of surface morphology on corrosion and electronic behavior. Acta Mater 2006;54:445–52. https://doi.org/10.1016/j.actamat.2005.09.017.
[7] Svahn F, Kassman-Rudolphi Å, Wallén E. The influence of surface roughness on friction and wear of machine element coatings. Wear 2003;254:1092–8. https://doi.org/10.1016/S0043-1648(03)00341-7.
[8] van Dam JPB, Abrahami ST, Yilmaz A, Gonzalez-Garcia Y, Terryn H, Mol JMC. Effect of surface roughness and chemistry on the adhesion and durability of a steel-epoxy adhesive interface. Int J Adhes Adhes 2020;96:102450. https://doi.org/10.1016/j.ijadhadh.2019.102450.
[9] Wingfield JRJ. Treatment of composite surfaces for adhesive bonding. Int J Adhes Adhes 1993;13:151–6. https://doi.org/10.1016/0143-7496(93)90036-9.
[10] Vasconcellos-Birro T, Paroissien E, Lachaud F, Aufray M. On the effect of roughness parameters on adherence using the three-point bending test (ISO 14679:1997). J Adhes 2022:1–26. https://doi.org/10.1080/00218464.2021.2024808.

[11] Rudawska A. Selected aspects of the effect of mechanical treatment on surface roughness and adhesive joint strength of steel sheets. Int J Adhes Adhes 2014;50:235–43. https://doi.org/10.1016/j.ijadhadh.2014.01.032.
[12] Şekercioğlu T, Rende H, Gülsöz A, Meran C. The effects of surface roughness on the strength of adhesively bonded cylindrical components. J Mater Process Technol 2003;142:82–6. https://doi.org/10.1016/S0924-0136(03)00463-1.
[13] Budhe S, Ghumatkar A, Birajdar N, Banea MD. Effect of surface roughness using different adherend materials on the adhesive bond strength. Appl Adhes Sci 2015;3:20. https://doi.org/10.1186/s40563-015-0050-4.
[14] Sourd X, Zitoune R, Crouzeix L, Coulaud M. Influence of the texturing quality consecutive to Abrasive Water Jet machining on the adhesive properties in mode I of 3D woven composite assemblies. Compos Part B: Eng 2022;242:110091. https://doi.org/10.1016/j.compositesb.2022.110091.
[15] Sills S, Overney RM. Probing Macromolecular Dynamics and the Influence of Finite Size Effects. In: Bhushan B, Fuchs H, editors. Applied Scanning Probe Methods III. Berlin, Heidelberg: Springer Berlin Heidelberg; 2006. p. 83–130. https://doi.org/10.1007/3-540-26910-X_4.
[16] ISO 25178–2, Geometrical product specifications (GPS), Surface texture: Areal, Part 2: Terms, definitions and surface texture parameters, (2021). https://www.iso.org/standard/74591.html.
[17] Yang D, Tang J, Xia F, Zhou W. Rough surface characterization parameter set and redundant parameter set for surface modeling and performance research. Materials 2022;15:5971. https://doi.org/10.3390/ma15175971.
[18] Reddy M VK, Kuriachen B, Joshy J, Joy ML. Influence of areal surface parameters on the tribological behavior of Ti6Al4V under lubricated condition. Tribology Int 2023;179:108147. https://doi.org/10.1016/j.triboint.2022.108147.
[19] Gualtieri E, Pugno N, Rota A, Spagni A, Lepore E, Valeri S. Role of roughness parameters on the tribology of randomly nano-textured silicon surface. J Nanosci Nanotech 2011;11:9244–50. https://doi.org/10.1166/jnn.2011.4296.
[20] Anwar S, Axinte DA, Becker AA. Finite element modelling of abrasive waterjet milled footprints. J Mater Process Technol 2013;213:180–93. https://doi.org/10.1016/j.jmatprotec.2012.09.006.
[21] Schwartzentruber J, Spelt JK, Papini M. Prediction of surface roughness in abrasive waterjet trimming of fiber reinforced polymer composites. Int J Mach Tools Manuf 2017;122:1–17. https://doi.org/10.1016/j.ijmachtools.2017.05.007.
[22] Kirk D, Abyaneh MY. Theoretical basis of shot peening coverage control. Shot Peen Mag 1995;(09).
[23] Bagherifard S, Ghelichi R, Guagliano M. On the shot peening surface coverage and its assessment by means of finite element simulation: A critical review and some original developments. Appl Surf Sci 2012;259:186–94. https://doi.org/10.1016/j.apsusc.2012.07.017.
[24] Maleki E, Unal O. Roles of surface coverage increase and re-peening on properties of AISI 1045 carbon steel in conventional and severe shot peening processes. Surf Interfaces 2018;11:82–90. https://doi.org/10.1016/j.surfin.2018.03.003.
[25] Vielma AT, Llaneza V, Belzunce FJ. Effect of coverage and double peening treatments on the fatigue life of a quenched and tempered structural steel. Surf Coat Technol 2014;249:75–83. https://doi.org/10.1016/j.surfcoat.2014.03.051.
[26] Taro M, Chaise T, Nélias D. A methodology to predict the roughness of shot peened surfaces. J Mater Process Technol 2015;217:65–76. https://doi.org/10.1016/j.jmatprotec.2014.10.016.
[27] Heydari Astaraee A, Bagherifard S, Monti S, Guagliano M. Evaluating the homogeneity of surface features induced by impact-based surface treatments. Materials 2021;14:3476. https://doi.org/10.3390/ma14133476.
[28] Senge JF, Astaraee AH, Dłotko P, Bagherifard S, Bosbach WA. Extending conventional surface roughness ISO parameters using topological data analysis for shot peened surfaces. Sci Rep 2022;12:5538. https://doi.org/10.1038/s41598-022-09551-9.
[29] Schubnell J, Eichheimer C, Ernould C, Maciolek A, Rebelo-Kornmeier J, Farajian M. The influence of coverage for high frequency mechanical impact treatment of different steel grades. J Mater Process Technol 2020;277:116437. https://doi.org/10.1016/j.jmatprotec.2019.116437.
[30] Sorrentino L, Parodo G, Turchetta S. CFRP laser texturing to increase the adhesive bonding: morphological analysis of treated surfaces. J Adhes 2021;97:1322–35. https://doi.org/10.1080/00218464.2020.1758074.
[31] Rivero A, Alberdi A, Artaza T, Mendia L, Lamikiz A. Surface properties and fatigue failure analysis of alloy 718 surfaces milled by abrasive and plain waterjet. Int J Adv Manuf Technol 2018;94:2929–38. https://doi.org/10.1007/s00170-017-0979-5.
[32] Hvizdos P, Zelenak M, Hloch S. Hardness and elasticity abrasive particles measured by instrumented indentation. MM SJ 2016;2016:869–71. https://doi.org/10.17973/MMSJ.2016_03_201601.
[33] Pedoto G, Grandidier J-C, Gigliotti M, Vinet A. Characterization and modelling of the PEKK thermomechanical and creep behavior above the glass transition temperature. Mech Mater 2022;166:104189. https://doi.org/10.1016/j.mechmat.2021.104189.
[34] Cenac F, Zitoune R, Collombet F, Deleris M. Abrasive water-jet milling of aeronautic aluminum 2024-T3. Proc Inst Mech Eng, Part L: J Mater: Des Appl 2015;229:29–37. https://doi.org/10.1177/1464420713499288.
[35] Chillman A, Ramulu M, Hashish M. A general overview of waterjet surface treatment modeling. Proc 2009 Am WJTA Conf 2009:B4.
[36] Meng P, Geskin ES, Leu MC, Li F, Tismeneskiy L. An analytical and experimental study of cleaning with moving waterjets. J Manuf Sci Eng 1998;120:580–9. https://doi.org/10.1115/1.2830162.
[37] Kirk D. Shot peening coverage: prediction and control. Shot Peen Mag 2009;(23).
[38] J. Tuszynski, Triangle/Ray Intersection, (2018). https://fr.mathworks.com/matlabcentral/fileexchange/33073-triangle-ray-intersection.
[39] Möller T, Trumbore B. Fast, minimum storage ray-triangle intersection. J Graph Tools 1997;2:21–8. https://doi.org/10.1080/10867651.1997.10487468.
[40] Blateyron F. The areal field parameters. In: Leach R, editor. Characterisation of Areal Surface Texture. Berlin, Heidelberg: Springer; 2013. p. 15–43. https://doi.org/10.1007/978-3-642-36458-7_2.
[41] Landis JR, Koch GG. The measurement of observer agreement for categorical data. Biometrics 1977;33:159–74. https://doi.org/10.2307/2529310.